


Supplementary Materials: The Influence of Mechanical Deformations on Surface Force Measurements

Romain Lhermerout* 

1. Models of contact mechanics

In this section, we briefly recall the hypotheses and consequences associated to the different models of contact mechanics, that are used to analyze the measurements (reviews can be found in [1–4]). All the models presented here rely on a common set of hypotheses or approximations. The two solid bodies in contact are supposed (i) semi-infinite, (ii) composed of linear (no plasticity) homogeneous (no stack of layers) isotropic (not crystalline) and purely elastic (no viscosity) materials, (iii) with perfectly smooth and frictionless surfaces, and (iv) in a regime where the contact radius is much smaller than their radius of curvature: $a \ll R$. These models differ in the way adhesion is taken into account. In the following, we consider the simple geometry of two cylinders of same radius of curvature R and material that are crossed at 90 degrees (or equivalently a sphere of radius of curvature R and a plane of same material), with the top solid controlled in position and the bottom solid mounted on a spring of stiffness k (see sketch in Figure 1(b)).

In Hertz model [5], it is hypothesized that there are no attractive forces between the surfaces (hard wall interaction, acting inside the contact area only). The normal force (or load) F , contact radius a and indentation δ (defined positive for compression and negative for dilatation) are related by:

$$\begin{cases} F = \frac{Ka^3}{R} \\ \delta = \frac{a^2}{R} \end{cases}, \quad (1)$$

where $K = \frac{2}{3} \frac{E}{1-\nu^2}$ is the elastic modulus, with E the Young's modulus and ν the Poisson's ratio. At lateral scale $|x| \ll R$, the distance z between the surfaces is given by:

$$z = \begin{cases} \frac{a^2}{\pi R} \left[\sqrt{\left(\frac{x}{a}\right)^2 - 1} + \left(\left(\frac{x}{a}\right)^2 - 2\right) \arctan \sqrt{\left(\frac{x}{a}\right)^2 - 1} \right] & \text{for } |x| \geq a \\ 0 & \text{for } |x| < a \end{cases}. \quad (2)$$

When moving up the top solid, the surfaces separate at $F_s = 0$, $a_s = 0$, $\delta_s = 0$, with no jump-out.

In Derjaguin-Muller-Toporov (DMT) model [6], attractive forces of finite range are added (sticky hard wall interaction, acting inside the contact area and in a ring-shaped zone outside the contact area), but adhesion is assumed not to deform the surfaces, leading to a discontinuity of the normal stress at the edge of the contact area. The normal force (or load) F , contact radius a and indentation δ are related by:

$$\begin{cases} F = \frac{Ka^3}{R} - 2\pi RW \\ \delta = \frac{a^2}{R} \end{cases}, \quad (3)$$

where W is the adhesion energy (per unit area, taken positive), and the deformation profile $z(x)$ is the same than in the Hertz model. When moving up the top solid, the surfaces separate at $F_s = -2\pi RW$, $a_s = 0$, $\delta_s = 0$, with a jump-out over a distance $2\pi RW/k$ due to the spring instability. Note that the relationship between the jump-out force and the adhesion energy coincides with the one given by the Derjaguin approximation [1,7],

33 because the surfaces are not deformed at the point of minimum force in the DMT model,
34 and supposed undeformable in the context of the Derjaguin approximation.

35 In Johnson-Kendall-Roberts (JKR) model [8], attractive forces of zero range are
36 added (Baxter i.e. infinitely short range square interaction, acting only inside the contact
37 area), and adhesion can deform the surfaces, leading to a divergence of the normal
38 stress at the edge of the contact area. The normal force (or load) F , contact radius a and
39 indentation δ are related by:

$$\begin{cases} F = \left[\sqrt{\frac{Ka^3}{R}} - \sqrt{\frac{3}{2}\pi RW} \right]^2 - \frac{3}{2}\pi RW \\ \delta = \frac{a^2}{R} \left[1 - \frac{4}{3} \left(\frac{a_s}{a} \right)^{3/2} \right] \end{cases}, \quad (4)$$

40 with $a_s = \left(\frac{3\pi R^2 W}{2K} \right)^{1/3}$. At lateral scale $|x| \ll R$, the distance z between the surfaces is
41 given by:

$$z = \begin{cases} \frac{a^2}{\pi R} \left[\sqrt{\left(\frac{x}{a} \right)^2 - 1} + \left(\left(\frac{x}{a} \right)^2 - 2 + \frac{8}{3} \left(\frac{a_s}{a} \right)^{3/2} \right) \arctan \sqrt{\left(\frac{x}{a} \right)^2 - 1} \right] & \text{for } |x| \geq a \\ 0 & \text{for } |x| < a \end{cases}. \quad (5)$$

42 When moving up the top solid, the surfaces separate at the point where $\frac{dF}{d\delta} = -k$. If
43 the spring constant is low enough, this condition can be approximated by $\frac{dF}{d\delta} = 0$, and
44 the surfaces separate at $F_s = -\frac{3}{2}\pi RW$, $a_s = \left(\frac{3\pi R^2 W}{2K} \right)^{1/3}$, $\delta_s = -\left(\frac{\pi^2 RW^2}{12K^2} \right)^{1/3}$, with a
45 jump-out over a distance $\frac{3}{2}\pi RW/k$.

46 In Maugis model [3], attractive forces of finite range d are added (Dugdale i.e.
47 square-well interaction, acting inside the contact area and in a ring-shaped zone outside
48 the contact area), and adhesion can deform the surfaces, leading to a normal stress that
49 presents no singularity at the edge of the contact area. The normal force (or load) F ,
50 contact radius a and indentation δ are related by implicit equations, together with a
51 dimensionless parameter here denoted as Ma :

$$Ma = \left(\frac{8RW^2}{\pi K^2 d^3} \right)^{1/3}. \quad (6)$$

52 Physically, Ma is the ratio between the elastic indentation due to adhesion and the
53 range of the attractive forces themselves. The three previous models are special cases
54 of Maugis model: Hertz limit corresponds to $Ma = 0$, DMT applies for $Ma \ll 1$, and
55 JKR is recovered for $Ma \gg 1$. In the transition regime $Ma \sim 1$, none of the DMT and
56 JKR models are valid and the implicit equations from Maugis model have to be used to
57 describe the contact mechanics.

58 2. Method for the determination of surface deformations

59 In this section, we explain in details the procedure of analysis of the FECO to deduce
60 the apical distance D and the geometry of the surfaces, i.e. the radius of curvature R and
61 the contact radius a (defined in Figure 1(b)). In general, the glue used to prepare the
62 surfaces is heterogeneous in thickness, leading to a local radius of curvature of mica that
63 is different from the radius of curvature of the supporting glass lens and differs from one
64 surface to the other (by typically $\sim 10\%$); therefore crossing the two cylinders at right
65 angle results in a contact zone of elliptic symmetry. During the experiments, we observe
66 the FECO along only one direction x parallel to the axis of symmetry of one lens (typical
67 FECO images for N_2 and $[C_4C_1\text{Pyrr}][\text{NTf}_2]$ cases shown in Figures 2(a) and 2(c)), that is
68 why to interpret the data we approximate the contact zone as a disk, i.e. we suppose
69 that the surface deformation is the same in the perpendicular direction y .

70 In (wavelength λ)-(lateral distance x) space first, we measure the shape $\lambda_p(x)$ of
 71 fringe of odd order p . For each line, the fringe position is detected by calculating the
 72 center of mass of the doublet (due to mica birefringence) after applying a threshold on the
 73 image (when the intensity is smaller than the threshold, it is set equal to the threshold).
 74 The threshold is chosen just above the intensity fluctuations of the background, to reduce
 75 the noise on the signal. Provided that the mica thickness is constant and known, the
 76 separation profile between the mica surfaces $z(x)$ can then be deduced (typical profiles
 77 for N_2 and $[C_4C_1Pyrr][NTf_2]$ cases shown in Figures 2(b) and 2(d)) [9]. The separation
 78 profile is measured up to a maximum scale $z_{\max} \sim 50 \text{ nm} \ll R \sim 1 \text{ cm}$, that is why the
 79 undeformed shape (when the surfaces are far from contact), circular in theory, is here
 80 observed locally and very well described by a parabola. There, a fitting procedure is used
 81 to extract D , R and a . On one hand, a parabolic fit is done at small scale close to the apex
 82 (green curve in Figure 2(b) and Figure 2(d)), with 3 free parameters, giving the apical
 83 distance D (negative in the present cases shown in the Figures, as explained in details
 84 in the next section). On the other hand, R and a are obtained with different methods,
 85 depending whether the solid surfaces are separated by N_2 or by $[C_4C_1Pyrr][NTf_2]$.

86 In the case of $[C_4C_1Pyrr][NTf_2]$, the mechanical deformations are limited to a
 87 scale $z \ll z_{\max}$, and the separation profile matches the undeformed shape at large
 88 measurable distances $z \sim z_{\max}$. A second parabolic fit is done at large scale only (blue
 89 curve in Figure 2(d)), with a function of the form:

$$z = z_0 + \frac{(x - x_0)^2}{2R}, \quad (7)$$

90 where x_0 and z_0 are 2 free parameters controlling the position of the parabola, and
 91 $R = 0.92 \pm 0.01 \text{ cm}$ is the radius of curvature that is adjusted using one image when the
 92 surfaces are far from contact and then kept fixed. By definition, the contact radius is
 93 the lateral distance $|x - x_0|$ at which the extrapolated undeformed profile crosses the
 94 contact plane at $z = D$, and is simply given by $a = \sqrt{2R(D - z_0)}$. To do this parabolic
 95 fit at large scale only, the points associated to values $|x - x_0| < a$ are excluded from the
 96 fit, and the fitting procedure is repeated iteratively: on first iteration no point is excluded
 97 and a value a_1 is deduced, on second iteration a_1 is used to exclude some points from
 98 the fit and a_2 is deduced, etc. In practice, 3 iterations are enough for the value of a to
 99 converge, as additional iterations lead to insensitive changes.

100 In the case of N_2 , the mechanical deformations turn to be present at all measurable
 101 scales $z \leq z_{\max}$, and the undeformed region of the profile cannot be observed. That is
 102 why the general definition of the contact radius a cannot be used, and a model is needed
 103 to fit the deformation. A fit of the separation profile is done at all measurable scales
 104 (blue curve in Figure 2(b)), with a function derived from the JKR model (equation 5):

$$z = \begin{cases} D + \frac{a^2}{\pi R} \left[\sqrt{\left(\frac{x - x_0}{a}\right)^2 - 1} + \left(\left(\frac{x - x_0}{a}\right)^2 - 2 + \frac{8}{3} \left(\frac{a_s}{a}\right)^{3/2} \right) \arctan \sqrt{\left(\frac{x - x_0}{a}\right)^2 - 1} \right], & \text{for } |x - x_0| \geq a \\ D & \text{for } |x - x_0| < a \end{cases}, \quad (8)$$

105 where the contact radius a and the center of the contact zone x_0 are 2 free parameters, the
 106 apical distance D is known from the small scale parabolic fit, the radius of curvature $R =$
 107 $0.92 \pm 0.01 \text{ cm}$ is adjusted using one image when the surfaces are far from contact and
 108 then kept fixed, and the contact radius at the jump-out point $a_s = 10.23 \mu\text{m}$ is adjusted
 109 using the image just before the jump-out of the surfaces and then kept fixed (see the
 110 corresponding FECO image and separation profile in Figure S1(a) and Figure S1(b)).

111 It is clearly visible in Figure 2(b) that the JKR model doesn't fit well the deformed
 112 profile at the edge of the contact zone, as it predicts a corner at right angle while the
 113 data exhibit a much smoother profile. The angular shape given by the JKR model is
 114 in fact non-physical, and is associated with the divergence of the normal stress at the

115 edge of the contact zone. This discrepancy was already mentioned in the seminal work
116 by Horn, Israelachvili and Fribac [2], where the smooth measured profile was thought
117 to be dominated by the flexural stiffness of the mica layer. This non perfect flattening
118 is therefore well known, but is highlighted here compared to previous studies (see
119 for example [10]) because of the use of a substantially thicker mica and of a sub-pixel-
120 detection technique to characterize the fringe profile. Nonetheless, we keep the JKR
121 fit as a first order determination of the contact radius, and we see in the main text that
122 this provides a variation of the contact radius with the force that is consistently well
123 described by the JKR model and an effective elastic modulus describing the layered solid
124 surfaces.

125 In order to obtain a reliable characterization of the geometry, note that all the images
126 had to be rotated by the same angle (of the order of the degree) before this analysis,
127 due to the fact that the camera is not perfectly aligned with the entrance slit of the
128 spectrometer and so the raw image is not ideally symmetric. One image, corresponding
129 to a situation when the surfaces are far from contact, is rotated by a given angle and the
130 separation profile is fitted at all scales with a parabola. The values of rotation angles are
131 scanned, and the optimum angle corresponds to the fit associated with the minimum
132 sum of squared residuals.

133 Finally, a is measured with a precision of $0.03 \mu\text{m}$ given by the standard deviation
134 of the signal, and an accuracy of $1 \mu\text{m}$ due to the uncertainty on the value of R (mainly
135 caused by the fact that the separation profile is observed up to a maximum scale $z_{\text{max}} \sim$
136 $50 \text{ nm} \ll R \sim 1 \text{ cm}$). This means that this method doesn't provide reliable values of a
137 when $a \lesssim 1 \mu\text{m}$, which is typically the case for $[\text{C}_4\text{C}_1\text{Pyrr}][\text{NTf}_2]$ under low loads.

138 In the literature, the measured force F is generally rescaled by the radius of cur-
139 vature R to compute an equivalent surface energy F/R , considering that mechanical
140 deformations are negligible and that the Derjaguin approximation applies. In the oppo-
141 site case when the surfaces are strongly flattened, it is reasonable to assume that the total
142 force F is mainly due to the interaction in the flattened region, and so to rescale it by the
143 contact area πa^2 to compute the mean local pressure $F/(\pi a^2)$. In this study, we explore
144 a broad range of situations from non measurable deformation to strong deformations,
145 that is why we have chosen to simply use the force F without any rescaling in the plots.

References

1. Israelachvili, J.N. *Intermolecular and Surface Forces (Third Edition)*; Academic Press, 2011. doi:10.1016/B978-0-12-375182-9.10010-7.
2. Horn, R.G.; Israelachvili, J.N.; Pribac, F. Measurement of the Deformation and Adhesion of Solids in Contact. *J. Colloid Interface Sci.* **1987**, *115*, 480–492. doi:10.1016/0021-9797(87)90065-8.
3. Maugis, D. Adhesion of spheres: The JKR-DMT transition using a dugdale model. *J. Colloid Interface Sci.* **1992**, *150*, 243–269. doi:10.1016/0021-9797(92)90285-T.
4. Grierson, D.S.; Flater, E.E.; Carpick, R.W. Accounting for the JKR-DMT transition in adhesion and friction measurements with atomic force microscopy. *J. Adhes. Sci. Technol.* **2005**, *19*, 291–311. doi:10.1163/1568561054352685.
5. Hertz, H. Ueber die Berührung fester elastischer Körper. *J. für die Reine und Angew. Math.* **1882**, *19*, p. 156. doi:10.1515/crll.1882.92.156.
6. Derjaguin, B.V.; Muller, V.M.; Toporov, Y.P. Effect of Contact Deformations on the Adhesion of Particles. *J. Colloid Interface Sci.* **1975**, *53*, 314–326. doi:10.1016/0021-9797(75)90018-1.
7. Derjaguin, B. Untersuchungen über die Reibung und Adhäsion, IV. *Kolloid-Zeitschrift* **1934**, *69*, 155–164. doi:10.1007/BF01433225.
8. Johnson, K.L.; Kendall, K.; Roberts, A.D.; Tabor, D. Surface energy and the contact of elastic solids. *Proc. R. Soc. A* **1971**, *324*, 301–313. doi:10.1098/rspa.1971.0141.
9. Israelachvili, J.N. Thin Film Studies Using Multiple-Beam Interferometry. *J. Colloid Interface Sci.* **1973**, *44*, 259–272. doi:10.1016/0021-9797(73)90218-X.
10. Israelachvili, J.N.; Perez, E.; Tandon, R.K. On the adhesion force between deformable solids. *J. Colloid Interface Sci.* **1980**, *78*, 260–261. doi:10.1016/0021-9797(80)90520-2.

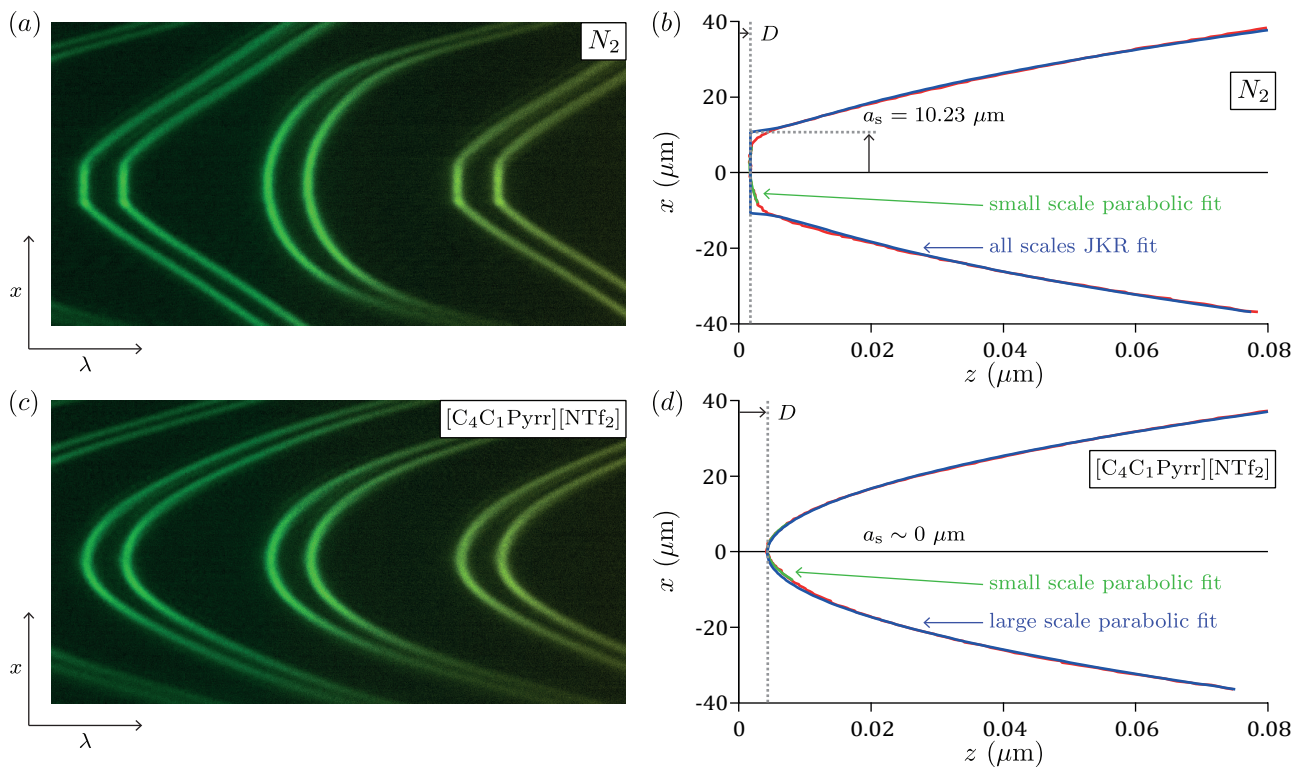


Figure S1. (a) Picture of the FCO when the two solid surfaces are in contact across N_2 , observed in (wavelength λ)-(lateral distance x) space. (b) Corresponding profile of the distance z between the surfaces along the lateral coordinate x (in red). A parabolic fit at small scale close to the apex (in green) allows to measure the apical distance D , while a fit with the JKR profile (equation 5 in main text) at all measured scales (in blue) is used to extract the contact radius a . (c) Picture of the FCO when the two solid surfaces are in contact across $[C_4C_1Pyrr][NTf_2]$, observed in (wavelength λ)-(lateral distance x) space. (d) Corresponding profile of the distance z between the surfaces along the lateral coordinate x (in red). A parabolic fit at small scale close to the apex (in green) allows to measure the apical distance D , while a parabolic fit at large scale (in blue) is used to extract the contact radius a . The two particular cases shown here correspond to the jump-out points reached in Figure 3 in main text.

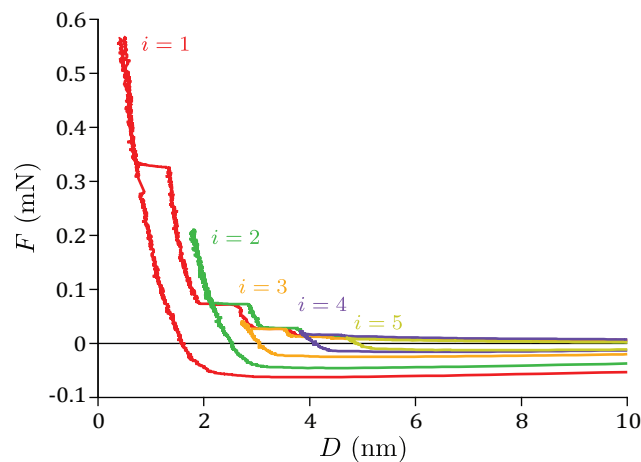


Figure S2. Force profile measured with $[C_4C_1Pyrr][NTf_2]$ between mica surfaces when approaching or retracting the top surface with the piezoelectric tube at $v = 0.5 \text{ nm/s}$, showing structuring with 5 distinguishable layers labeled by i . The different colors stand for approach up to a given layer and retraction from this layer: $i = 1$ in red, $i = 2$ in green, $i = 3$ in orange, $i = 4$ in purple, and $i = 5$ in yellow.

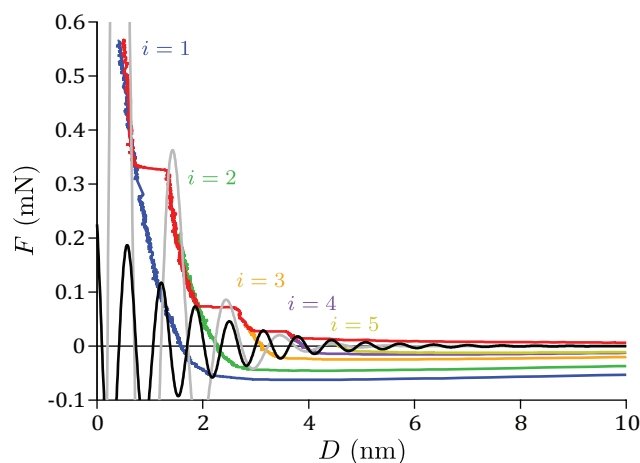


Figure S3. Force profile measured with $[C_4C_1\text{Pyrr}][\text{NTf}_2]$ between mica surfaces when approaching or retracting the top surface with the piezoelectric tube at $v = 0.5 \text{ nm/s}$, showing structuring with 5 distinguishable layers labeled by i . For clarity, only the full approach is shown (in red), together with retractions from layers $i = 1$ (in blue), $i = 2$ (in green), $i = 3$ (in orange), $i = 4$ (in purple), $i = 5$ (in yellow). The gray curve is an exponentially decaying harmonic oscillation (equation 10 in main text) with parameters $F_0 = F_0^{\max}$, $D_0 = D_0^{\max}$, $\zeta = \zeta^{\max}$ and $\lambda = \lambda^{\max}$ obtained from the fits of the points of maximum force. The black curve is an exponentially decaying harmonic oscillation (equation 10 in main text) with parameters $F_0 = F_0^{\min}$, $D_0 = D_0^{\min}$, $\zeta = \zeta^{\min}$ and $\lambda = \lambda^{\min}$ obtained from the fits of the points of minimum force (see equations 11 and 12, and Figures 4(b) and 4(c) in main text).